

Metasurface-enhanced multifunctional flag nanogenerator for efficient wind energy harvesting and environmental sensing



Liwei Dong^{b,c}, Guobiao Hu^d, Ye Zhang^e, Wei Ding^{c,f}, Shuai Qu^{c,g}, Qian Tang^h, Chaoyang Zhao^c, Yaowen Yang^{c,*}, Fan Yang^{a,*}

^a Department of Orthopaedics, Shanghai Key Laboratory for Prevention and Treatment of Bone and Joint Diseases, Shanghai Institute of Traumatology and Orthopaedics, Ruijin Hospital, Shanghai Jiao Tong University School of Medicine, Shanghai 200025, China

^b Institute of Rail Transit, Tongji University, Shanghai 201804, China

^c School of Civil and Environmental Engineering, Nanyang Technological University, 50 Nanyang Avenue, Singapore 639798, Singapore

^d Internet of Things Thrust, The Hong Kong University of Science and Technology (Guangzhou), Nansha, Guangzhou, Guangdong 511400, China

^e School of Mechanical and Power Engineering, Zhengzhou University, Zhengzhou 450000, China

^f School of Mechanical Engineering, Xi'an Jiaotong University, Xi'an, Shaanxi 710049, China

^g Train and Track Research Institute, State Key Laboratory of Traction Power, Southwest Jiaotong University, Chengdu 610031, China

^h Chongqing Key Laboratory of Green Energy Materials Technology and System, Chongqing University of Technology, Chongqing 400054, China

ARTICLE INFO

Keywords:

Wind energy harvesting
Triboelectric nanogenerator
Metasurface
Self-powered sensing
Flow-induced vibration

ABSTRACT

Wind energy, as a widely distributed and renewable energy resource, plays a crucial role in promoting self-powered wireless sensor networks and wind speed sensing. However, current research predominantly focuses on specific application purposes, lacking comprehensive investigations into integrated solutions. In this paper, a metasurface-enhanced multifunctional flag-type triboelectric nanogenerator (FTENG) is introduced, which enables efficient wind energy harvesting as well as accurate wind speed sensing over a wide range of wind speeds via the synergistic effect of metasurface treatment on the flagpole and flexible flag fixation approach. The flexible fixation maximally utilizes the upstream wake of metasurface configurations, boosting the energy harvesting power density by up to 23 times. The metasurface-enhanced FTENG with careful optimization, striking a balance between energy harvesting and sensing capabilities, achieves a linearity of 0.992 over a wind speed range of 2.3–14.4 m/s and a peak power density of 250 mW/m². Finally, the FTENG demonstrates its excellent abilities to light LEDs, power the wireless sensor node (WSN), and serve as a self-powered environmental sensor. This work opens up an impactful possibility for developing versatile self-powered electronics by employing metasurface-enhanced wind energy harvesting techniques.

1. Introduction

The rapid evolution and widespread expansion of the Internet of Things (IoTs) have led to an unprecedented surge in the demand for sensors. In light of extensive sensor deployment, conventional battery-powered solutions not only confront the necessity of periodic manual maintenance but also engender a proliferation of hazardous wastes, thereby constituting a substantial environmental issue. Fortunately, over the past decade, we have witnessed the development of energy harvesting technologies, encompassing wind [1], mechanical [2], thermal [3] and solar energy harvesting [4], and they have achieved tremendous success in the fields of ocean engineering [5,6], road engineering [7–9], aerospace engineering [10], and smart wearables [11],

[12]. Given that wind energy is a widely available and abundant renewable energy source, wind energy harvesting remains an enduring area of research interest for scholars.

Electromagnetic and piezoelectric mechanisms have traditionally served as primary means for wind energy harvesters (WEHs) in their initial designs [13]. Since the concept of triboelectric nanogenerators (TENGs) was proposed in 2012 [14], their diverse working modes offer more possibilities for the miniaturization and diversification of WEHs. From the perspective of dynamics, the principles for WEHs can be classified as rotation [15–17] and flow-induced vibration (FIV) [18]. Rotary wind energy harvesters (RWEHs) typically leverage components such as wind cups or wheels to convert wind flow into rotational mechanical energy, which is subsequently transformed into electricity by

* Corresponding authors.

E-mail addresses: cwyang@ntu.edu.sg (Y. Yang), yf12498@sjtu.edu.cn (F. Yang).

harnessing various energy harvesting mechanisms. For instance, Tairab et al. [19] integrated solar panels into an electromagnetic rotary RWEH, achieving an average electric output of 3.2 W and 20.5 mW for solar and electromagnetic parts respectively. Cao et al. [20] successfully employed piezoelectric cantilevers in an RWEH with the magnetic coupling, and the resistance torque can be reduced by 33% as well as a peak power of 22.2 mW can be realized with optimal magnet arrangement. Zhao et al. [21] proposed another magnet coupling approach with a force amplification mechanism to enable a higher equivalent piezoelectric performance. This design demonstrated an effective operational range of 3–10 m/s and superior durability. TENGs have emerged as reliable candidates for wind energy harvesting, due to their cost-effectiveness, flexibility, simple structure, and diverse working modes. Most TENG-based RWEHs operate under the lateral-sliding mode, and researchers consistently enhance their charge density with advanced approaches including microstructures [22], charge pumps [23], environmental control [24], and air breakdown effect [25]. Non-contact designs have also been proposed for TENG-based RWEHs to mitigate interface heat and wear [26]. Additionally, the hybridization of two or three energy conversion mechanisms has been validated as an effective approach to enhance their robustness and power density [27–29]. The innate advantage of rotary structures is their capacity for omnidirectional wind energy harvesting, while, higher driven wind speeds over 3–4 m/s are accompanied owing to their inertia and static friction of moving components [30].

FIV stands as a prevalent physical phenomenon in engineering, arising from aerodynamic instability or vortex shedding when a fluid interacts with a slender structure. The use of FIV structures has become a promising approach for small or micro-scale WEHs to harness energy from wind/ liquid flows [31]. In contrast to rotary structures, FIV-based WEHs exhibit the potential to attain smaller cut-in wind speeds, thanks to their more flexible and adaptable configurations [32]. Diverse FIV mechanisms exist, categorized as vortex-induced vibration (VIV) [33], waking galloping [34], galloping [35], and fluttering [36]. The first two are characterized as forced vibrations typically induced by the wakes generated by a bluff body located at the front end or arranged in front of harvesters [37,38]. In the lock-in zone, the structure vibrates with the vortex shedding frequency, resulting in significant energy output, but is limited by a narrow operating bandwidth. The latter two phenomena can be characterized as limit cycle oscillations, typically triggered at higher wind speeds, concurrently offering a broader operational wind speed range. The cross sections of bluff bodies have a remarkable impact on overall efficiency and energy output, even altering the forms of FIV [39]. Liu et al. [40] proposed a double-airfoil bluff body that can passively adjust VIV and galloping when subject to time-varying environmental wind. Fluttering WEHs, often taking the extrinsic form of flags, present a compact, flexible, and easily deployable approach to wind energy harvesting. These devices are typically fabricated using triboelectric or flexible piezoelectric materials. In the case of triboelectric flag-type WEHs, two triboelectric materials with opposing electron affinities are interwoven or glued together to form the flag body [41,42]. In addition, the flapping behavior between two flags [43], as well as the flapping of the flag with one or two lateral baffles [44], create contact and separation opportunities for triboelectric energy harvesting. Typically, a bluff body configured in front of flag-type WEHs can enhance their performance and extend their operational range [45]. For instance, Latif et al. [46] demonstrated the bluff body with 120-degree concave can maximize the wind energy harvesting efficiency of piezoelectric flags. Dong et al. [47] innovatively integrated the flapping piezoelectric flag as a distinctive bluff body with a fluttering triboelectric flag, and utilized the flag flapping wake to boost the performance of the triboelectric flag. Han et al. [48] proposed a lateral oscillation bluff body with, doubling the generated electric power of the triboelectric flag.

WEHs with broad operational wind speed ranges hold the potential to function as wind speed sensors [49,50]. Wang et al. [51] developed a flag-type nanogenerator for wind speed sensing, achieving an

operational range of 3–7.5 m/s. Yao et al. [52] conceived an innovatively TENG-based wind speed sensor with an arc-shaped structure, which realizes a striking fitness R^2 of 0.998 between the flutter frequency and wind speed over a range of 6–20 m/s. Xu et al. [53] combined an angle-sharped TENG with a wind vane and photoelectric technology for concurrently monitoring wind speed and direction. The proposed TENG can detect the wind speed in eight directions, while also possesses a maximum output of 2.06 μ W for self-powered applications. Ko et al. [54] devised a TENG with a curved flap array, enabling omnidirectional wind speed sensing across the range of 1.5–10 m/s. Furthermore, Yu et al. [55] utilized the charge-excitation strategy and a novel elastic mechanism weakening the impacts of humidity and other environmental factors on voltage output.

FIV-based WEHs have demonstrated substantial promise in both wind energy harvesting and speed sensing domains. However, TENGs employed for wind speed sensing often exhibit moderate performance, limiting their potential as a sustainable power supply. The integration of dual functionalities within a single TENG could dramatically enhance the practicality: the wind speed sensing module would accurately measure wind velocity, while the energy harvesting component could capture wind energy to power wireless communication modules and environmental sensors (e.g., for temperature and humidity), thereby creating a self-powered multifunctional environmental sensing system. Yet, advancing FIV-based TENGs towards this goal faces several significant obstacles: (1) a deficiency in the development of mechanisms or configurations tailored for multifunctional applications, crucial for the efficacy of integrated systems; (2) a lack of thorough investigation into aerodynamics and metasurface designs, which are essential for optimizing wind energy harvesting capabilities; (3) the absence of a comprehensive design framework for multifunctional TENGs, informed by systematic analysis of parameters, which is vital for guiding the development and enhancing the functionality of these systems. Addressing these challenges is essential for the progression of wind energy harvesting technology and the realization of autonomous environmental monitoring systems.

Thus, this paper introduces a novel approach to address the limited output of TENGs, aiming to achieve high-performance multifunctional TENGs. A wind-driven flag-type TENG (FTENG) is developed, and innovative metasurface designs on the flagpole, along with a flexible fixing approach, are proposed to simultaneously enhance wind energy harvesting and guarantee high-linearity wind speed sensing. A total of 12 metasurface designs incorporating both convex and concave surface designs are comprehensively compared in wind energy harvesting and speed sensing, and corresponding optimization strategies are proposed with the consideration of metasurface parameters and FTENG structural parameters. In addition, the vorticities generated by the metasurface flagpole are simulated to visually reveal the impact of the metasurface on the surrounding flow field. Among various candidates, an optimized FTENG attains a linearity of 0.992 with a wind speed sensing range of 2.3–14.4 m/s, and achieves a peak power density of over 250 mW/m² in wind energy harvesting. In demonstration tests, the FTENG exhibits the capacity of lighting 100 LEDs in series, and powers a WSN implementing mobile temperature monitoring. It also showcases its rapid response and prediction accuracy as a wind speed sensor. These results collectively highlight the promising potential of metasurface designs in advancing the practicality and functionality of TENGs in the domains of energy harvesting and smart sensing.

2. Results and discussion

2.1. Structure and working principle of FTENG

The FTENG comprises a flag body and baffles on both sides, as illustrated in Fig. 1a. The flag body incorporates a PTFE membrane and a flagpole featuring the metasurface design. When the wind flows from the leading end of the flag to its rear end, the flag made of the PTFE

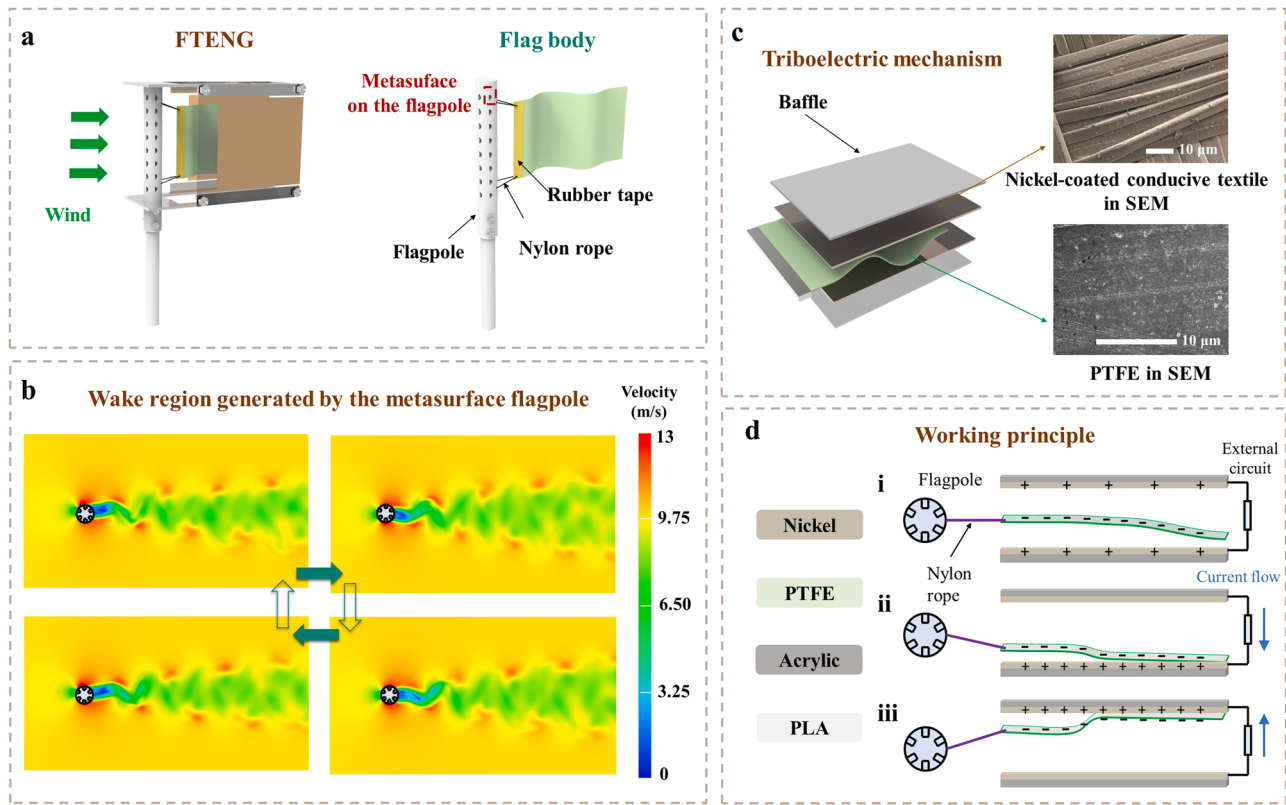


Fig. 1. Structure and working principle of FTENG: (a) overall configuration of FTENG; (b) wake region generated by the flagpole with a metasurface design in one period of vortex shedding; (c) materials of FTENG and their photographs in SEM; (d) free-standing working mode of FTENG.

membrane undergoes fluttering, and will contact or separate from the conductive textile with nickel coating attached on the inner side of the baffles. The metasurface design on the flagpole can generate stronger wake effects at the rear end of the flagpole, intensifying the flag fluttering. Meanwhile, to leverage the upstream wake, the flag is connected to the flagpole with nylon ropes. The wake region of a metasurface flagpole is illustrated in Fig. 1b. The dynamic behavior of nylon rope and flag will be dominated by the wakes behind the flagpole, which can be categorized as the wake galloping effect. The flag leading edge fixed with the nylon rope will oscillate laterally at a certain angle under the upstream wakes, thus increasing the contact area with the conductive textile. The microstructures of two materials for triboelectrification are captured by the scanning electron microscope (SEM) in Fig. 1c. The FTENG operates in the freestanding working mode for wind energy harvesting, as depicted in Fig. 1d. At the beginning, the PTFE membrane hangs slightly due to gravity, and keeps out of contact with the conductive textile on both sides (see Fig. 1d-i). As the wind flows across the PTFE membrane, it will be excited to flutter and come into contact with the lower electrode. Then, positive charges will transfer from the lower electrode to the upper one, along with a transient current generated (see Fig. 1d-ii). Conversely, when the PTFE membrane comes into contact with the upper electrode, the transfer direction of positive charges and accompanying transient current will be reversed (see Fig. 1d-iii). To deal with wind direction changes in the natural environment, FTENG can be integrated with a wind vane to achieve automatic alignment with the wind direction. As shown in Fig. S1, a wind vane is rigidly connected to the flagpole, with the flagpole's end embedded into a stationary base equipped with a bearing mounting. When the FTENG is confronted with substantial variations in wind direction, the wind vane will automatically align with the wind direction and simultaneously drive the flagpole and FTENG to move synchronously with it, ensuring continuous and effective operation of the FTENG.

In the freestanding working mode, the generated voltage of FTENG can be governed as [56]

$$V = -\frac{1}{C}Q + V_{oc} = -\frac{T_0 + D_0}{\epsilon S} + \frac{2\sigma x}{\epsilon} \quad (1)$$

where C denotes the capacitance of the FTENG; Q is the total transferred charge; V_{oc} is the open-circuit voltage; T_0 and D_0 represent the PTFE membrane thickness and the distance between two baffles; ϵ is the dielectric constant in a vacuum; S refers to the effective electrode area involved in contact; x represents the relative displacement between the PTFE membrane and the baffle; and σ denotes the charge density. Eq. (1) indicates the performance of FTENG in the freestanding working mode is relevant to the PTFE membrane thickness, the distance between two baffles, the effective electrode area and the relative displacement. The effective electrode area is determined by the flag motion state. The relative displacement x depends on the wind speed, the distance between two baffles, flag geometric parameters and material characteristics. Relevant variables will be considered for the performance optimization of FTENGs in subsequent sections.

2.2. Influence of flexible fixing on flag characteristics

The PTFE flag is connected to the flagpole with a nylon rope, as illustrated in Fig. 2a. This flexible fixing design offers two main advantages: (1) the nylon rope maintains a certain distance between the flag and the flagpole, facilitating the utilization of upstream wakes; (2) the leading edge of the flag will undergo periodic lateral vibration driven by upstream wakes, increasing the contact area with conductive textiles and improving the generated voltage. In this section, the superiority of flexible fixing is demonstrated through a series of wind tunnel tests. The test setup is provided in Fig. S2, and the results are illustrated in Fig. 2. As the fluttering frequency depicted in Fig. 2b and c, the first advantage of the flexible fixing is the cut-in speed of FTENG declining

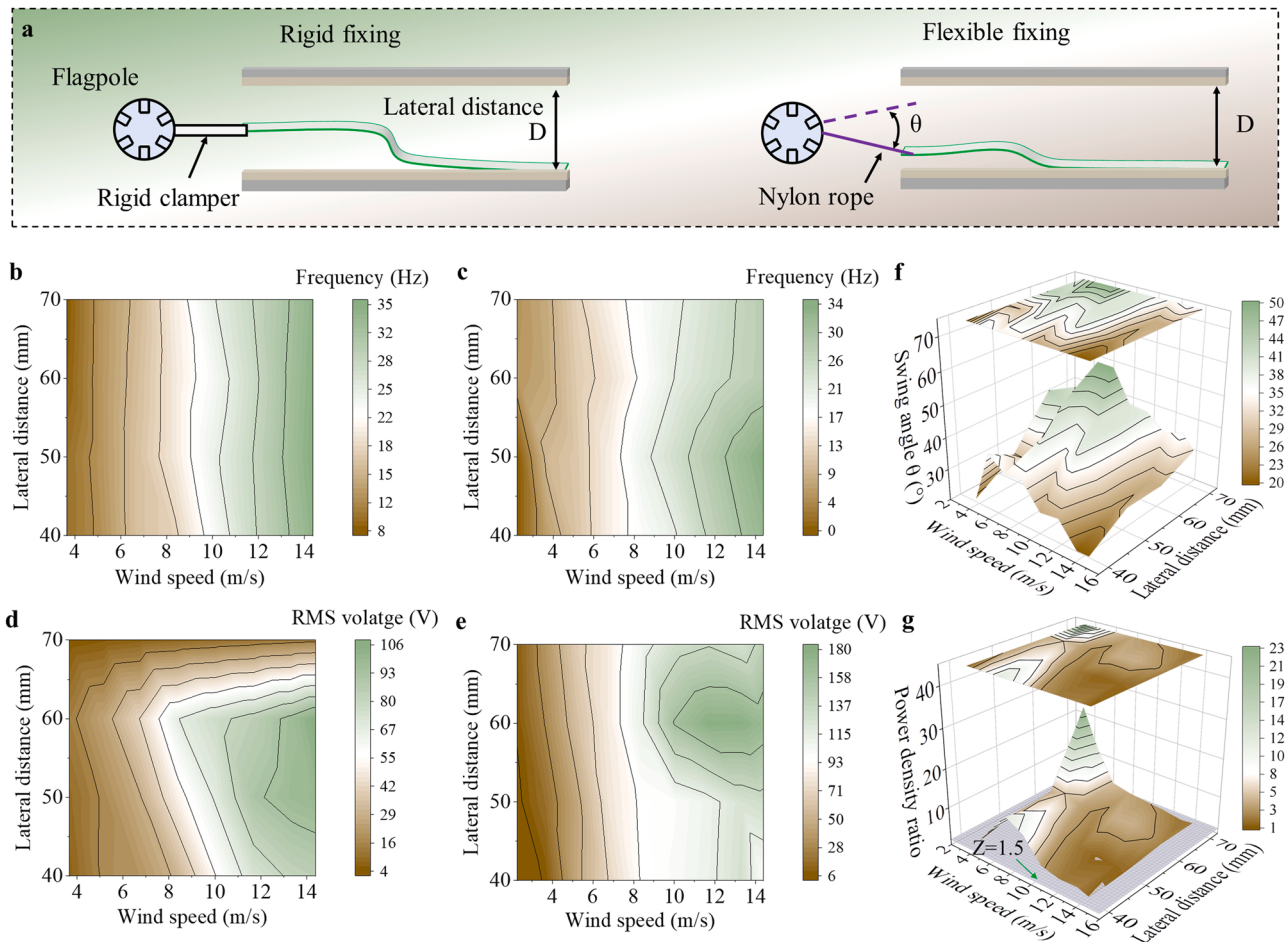


Fig. 2. Comparison of two types of connection approaches for FTENG: (a) schematic of two connection approaches; (b) fluttering frequency of FTENG with rigid fixing and (c) flexible fixing versus lateral distance and wind speed; (d) RMS voltage of FTENG with rigid fixing and (e) flexible fixing; (f) swing angle of rope and (g) power density improvement (the flag length is 100 mm).

from 3.67 to 2.27 m/s, which is a benefit to improve the low-speed wind energy harvesting and a broader operational range for wind speed sensing. Herein, the lateral distance D is considered as a variable because it is a key factor that affects the airflow flowing to the inner sides of baffles as well as the contact behavior between the PTFE membrane and electrodes. The variation in the lateral distance D under rigid fixing hardly has an impact on the fluttering frequency at the corresponding wind speed, while the fluttering frequency at high wind speeds over 10 m/s declines with an increased lateral distance D under flexible fixing. Nevertheless, a common feature is that the flutter frequency is generally positively correlated with the wind speed. Fig. 2d and e compared the voltage performances of the two configurations. The high-performance region for rigid fixing is located in a high wind speed range of 10–14 m/s and a lateral distance D of 45–65 mm. For flexible fixing, the high-performance region shifts upwards, and the lateral distance D of 50–70 mm is more conducive for power generation. It is noted that the overall voltage performance with flexible fixing is better than that with rigid fixing, with the maximum root mean square (RMS) voltage reaching 180 V, about 70% increase compared to 106 V. This is attributed to the lateral swing of the leading edge of the PTFE membrane. The swing angle is illustrated in Fig. 2f, and the power density improvement is demonstrated in Fig. 2g. A larger swing angle occurs in the wind interval of 6–8 m/s, gradually decreasing when deviating from this range. At low wind speeds, the PTFE membrane flutter slightly, resulting in a minor swing angle. Due to the high fluttering frequency of the PEFE membrane at high wind speeds and the hysteresis of nylon rope swinging, the swing direction will be quickly switched, also leading to a

minor swing angle. The maximum swing angle is maximum at 60 mm with the variation in the lateral distance. Correspondingly, the most substantial boost in power density occurs at 6–8 m/s and the lateral distance around 60 mm, achieving a maximum improvement of up to 23 times. This demonstrates the significant enhancement in energy harvesting capacity at low and moderate wind speeds with the proposed flexible fixing approach.

2.3. Metasurface designs on the flagpole

To offer a straightforward and implementable approach to enhance the performance of FTENG, this section explores and compares various metasurface designs on a cylinder flagpole. The flagpole diameter and metasurface parameters including characteristic diameter, depth/height, and density have been optimized based on the test results in Figs. S3 and S4, and relevant discussions are supplemented in Note S1. In Fig. 3a, 12 types of metasurfaces are designed, and 6 of them feature convex surface designs and the other 6 are characterized by concave surface designs. The electrical output of FTENG with different metasurfaces is illustrated in Fig. 3b, and the corresponding instantaneous voltage curves versus wind speed are provided in Fig. S5. Most convex metasurfaces hardly improve the power generation performance of FTENG, except that Configuration B1 achieves a maximum RMS voltage of 145.9 V and showcases the most remarkable overall performance improvement. The instantaneous voltage comparison between Configurations B1 and X is illustrated in Fig. 3d. On the contrary, most concave metasurfaces contribute to varying degrees of improvement in

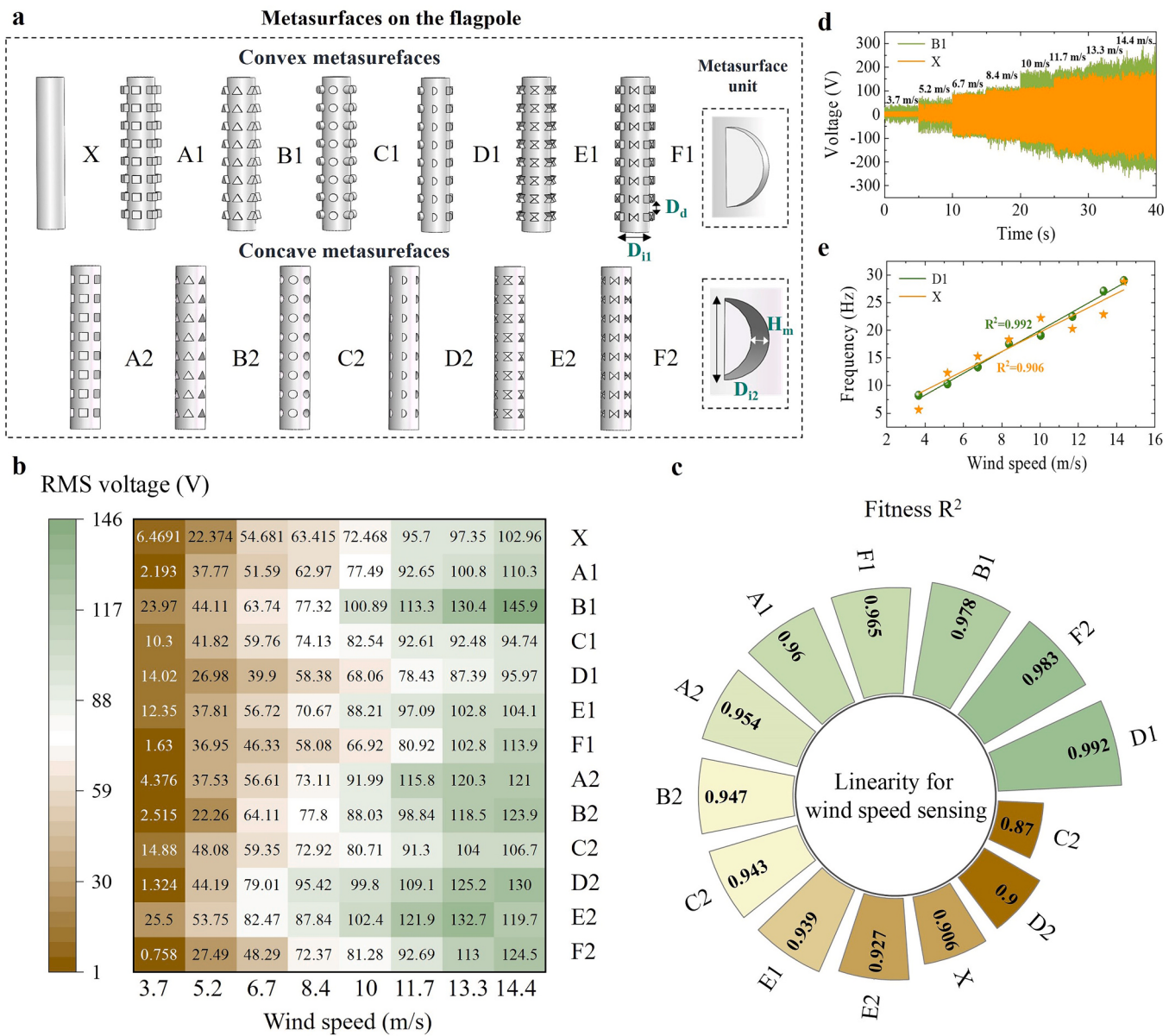


Fig. 3. Comparison of different metasurfaces for the perspective of wind energy harvesting and speed sensing: (a) 12 types of metasurfaces on the flagpole including convex and concave surface designs; (b) RMS voltage with different metasurface designs; (c) linearity of the flag fluttering frequency versus wind speed characterized by fitness R^2 ; (d) instantaneous voltage of Configurations B and X; (e) flag fluttering frequency curve of Configurations D1 and X (the flag length is 100 mm, and the lateral distance is 50 mm).

the generated RMS voltage values. Thus, from the perspective of energy harvesting, the concave metasurface designs emerge as the preferred choice.

Given the susceptibility of FTENG voltage performance to environmental humidity, a more reliable method for monitoring wind speed involves analyzing the flag fluttering frequency. This frequency corresponds to the dominant frequency of the voltage signal under Fast Fourier Transform (FFT). The linearity of the wind speed sensor is evaluated by calculating the fitness of the first-order function between the dominant frequency and wind speed. The linearity rankings for diverse configurations are depicted in Fig. 3c. Notably, Configuration D1 attains the highest linearity of 0.992, while Configuration C2 exhibits a linearity of 0.87, even inferior to Configuration X. The flag fluttering frequency with Configurations C2 and X is intuitively compared in Fig. 3e. An interesting phenomenon is that the configurations with the highest linearity predominantly feature convex metasurface designs, whereas concave metasurface designs excel in enhancing power

generation capability. This indicates the necessity of metasurface designs in alignment with the primary function and purpose of FTENGs.

2.4. Metasurfaces for wind speed sensing

To harness the functional advantages of metasurfaces in improving the linearity of wind speed sensing, parametric analysis is imperative to explore optimal parameters for various metasurface configurations. Fig. 4a outlines a proposed parametric optimization process. The first step is the selection of the metasurfaces conducive to wind speed sensing. Based on the linearity ranking in Fig. 3, Configurations D1, B1 and F2 showcase great potential in wind speed sensing, and are thus chosen as candidates. Subsequently, an expansive operational wind speed range of FTENG is beneficial for a broader spectrum of wind speed sensing. Flags in ambient wind can be simplified as thin plates in uniform flow during dynamic investigations. The softness of flags is characterized by low bending rigidity, and the main restoring force arises

a Metasurfaces on the flagpole for wind speed sensing

- Step 1 Choose three metasurfaces with good linearity for wind speed sensing purposes
Determine metasurface
- Step 2 Explore the influences of flag thickness and length on linearity and operating wind speed range
Determine thickness and length
- Step 3 Study the influence of lateral distance on linearity
Determine lateral distance
- Step 4 Obtain optimal linearity of metasurfaces and their optimal parameters

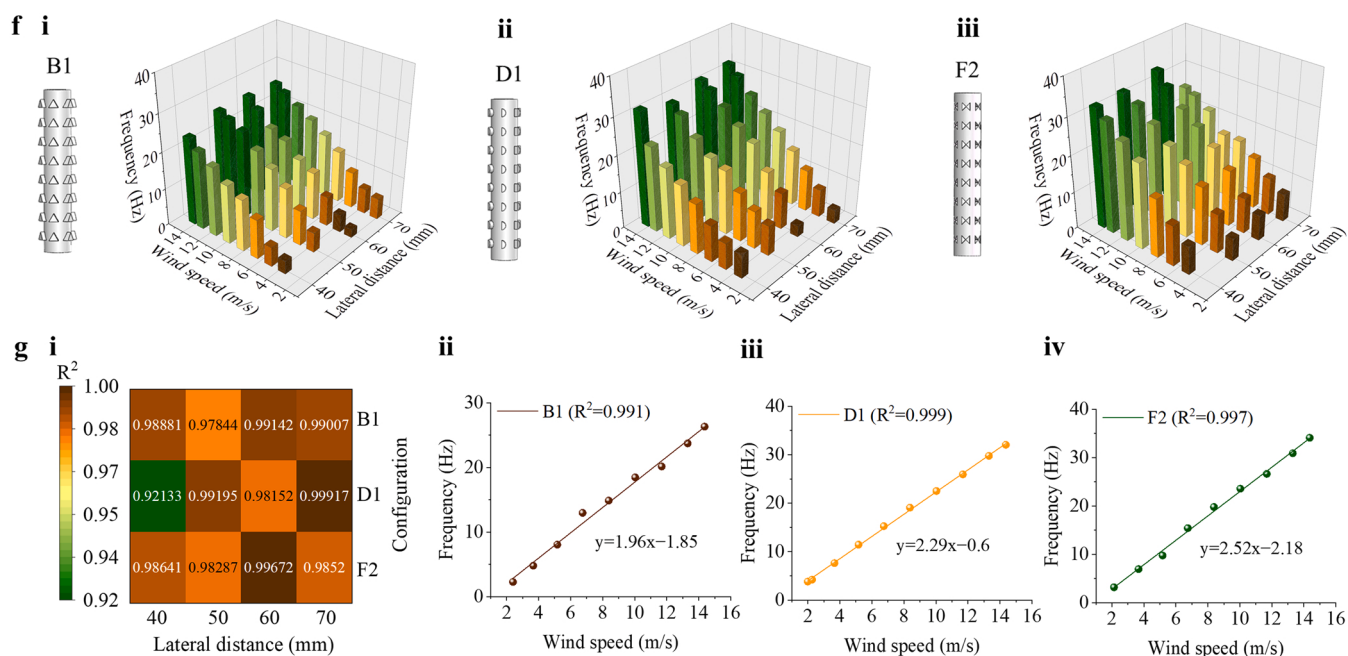
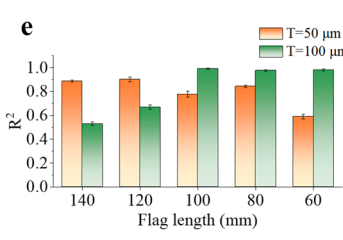
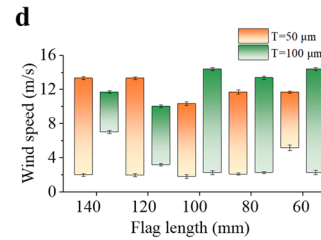
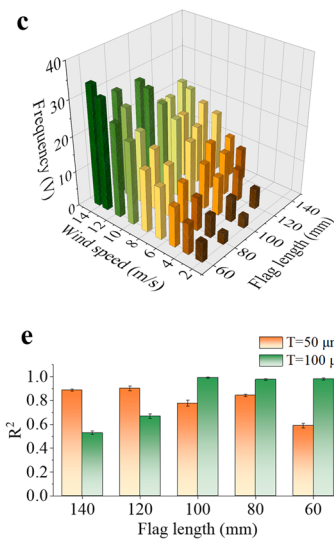
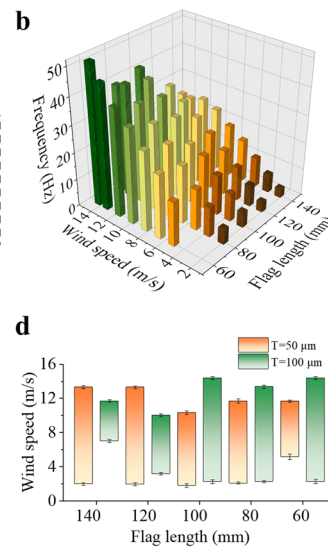
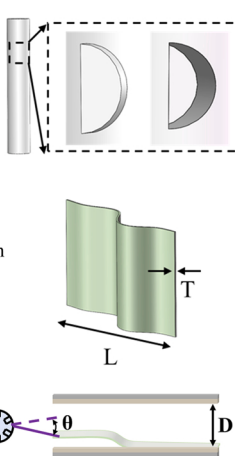


Fig. 4. Metasurfaces on the flagpole for wind speed sensing: (a) optimization process for FTENGs with metasurfaces towards high-linearity wind speed sensing, (b) fluttering frequency versus wind speed and flag length with 50 μm and (c) 100 μm thickness; (d) operational wind speed range and (e) fitness R^2 versus flag length and thickness (Configuration D1); (f) fluttering frequency of Configurations B1, D1 and F2 versus lateral distance; (g) fitness R^2 versus lateral distance and optimal fluttering frequency-wind speed curves for three configurations (the flag height is constant 70 mm).

from the flow-induced tension [57]. Their fluttering patterns are inherently associated with mass ratio M^* , aspect ratio H^* , non-dimensional bending Stiffness K_b , Reynolds number R_e , and gravity [58]:

$$M^* = \frac{\rho_s T}{\rho_f L} \quad (2)$$

$$K_b = \frac{ET^3}{12(1-\nu^2)\rho_f U^2 L^3} \quad (3)$$

$$R_e = \frac{\rho_f UL}{\mu} \quad (4)$$

$$H^* = \frac{H}{L} \quad (5)$$

where ρ_f and ρ_s denote the air and solid densities; T and L are the flag thickness and length; E represents Young's modulus; ν refers to the Poisson's ratio; U represents the wind speed; μ is the air viscosity; H refers to the flag height.

Therefore, the investigation of flag fluttering characteristics necessitates consideration of factors such as flag thickness, flag length, and wind speed. Taking Configuration D1 as an example, the influence of different lengths (60–140 mm) and wind speeds (0–15 m/s), while maintaining a constant flag thickness of 0.05 mm, on the fluttering frequency is depicted in Fig. 4b. The fluttering frequency rises with an increased wind speed and a declined flag length, and achieves a maximum value of 50 Hz with a flag length of 60 mm at 14.4 m/s. This trend is attributed to the decrease in flag length leading to an increase in the mass ratio, consequently resulting in a higher fluttering frequency [58]. In Fig. 4c, with a constant flag thickness of 0.1 mm, the fluttering

frequency is observed to be lower than that with a thickness of 0.05 mm under equivalent flag length and wind speed conditions, which is attributed to a higher mass ratio associated with an increased flag thickness. Fig. 4d and e summarizes the effective operational wind speed range and fitness R^2 versus the flag length (mass ratio). Herein, the effective upper critical speed accounts for the criticality at which the flutter frequency begins to decrease with an increased wind speed. Due to the intensification of chaotic phenomena in the flag fluttering at high Reynolds numbers R_e , as well as the impact of metasurfaces on the flow field around the flag, the flag fluttering frequency may not increase monotonically when the wind speed exceeds a critical point, which is unfavorable for FTENGs towards a broadband wind speed sensing. When the flag thickness is 0.05 mm, a softer flag body tends to flutter chaotically at lower wind speeds, resulting in generally lower effective upper critical speeds compared to a flag thickness of 0.1 mm. Meanwhile, a smaller cut-in speed of 1.97 m/s is realized as a result of the reduced gravity that the lift needs to overcome, and it hardly changes with the flag length until the length decreases to 60 mm. For flags with a thickness of 0.1 mm, the cut-in speed gradually decreases to 2.27 m/s with the flag length reducing from 140 to 100 mm, as a result of the attenuation of gravity. When the length ≤ 100 mm, they generally achieve a favorable operational wind speed range. The fitness R^2 denotes the linearity of the fluttering frequency with the wind speed, where a higher

linearity corresponds to a broader effective operational range in most conditions. The highest linearity of 0.992 over an operational range of 2.27–14.4 m/s is attained in Fig. 4e when the flag length is 100 mm and the thickness is 0.1 mm.

Further optimization of the three metasurface designs with this flag parameter configuration is conducted, and the flag fluttering frequency versus wind speed and lateral distance D is illustrated in Fig. 4f. It is noted that a smaller lateral distance has the potential to render the flag unresponsive at low wind speeds, leading to an increased cut-in speed. By comparing the three metasurface configurations, it can be found that the flutter frequency increases sequentially from left to right, which also demonstrates the intuitive impact of metasurface configurations on the flow field around the flag and the flag dynamic response. As depicted in Fig. 4g, except the Configuration D1 with a lateral distance of 40 mm, most conditions achieve a good fitness over 0.95. Even with an optimal lateral distance, the fitness for three configurations all exceeds 0.99, as illustrated in Fig. 4g-ii to iv, respectively. Additionally, the average power densities for three configurations versus lateral distance are presented in Fig. S6.

2.5. Metasurfaces for wind energy harvesting

The results presented in Fig. 3 underscore the significant potential of

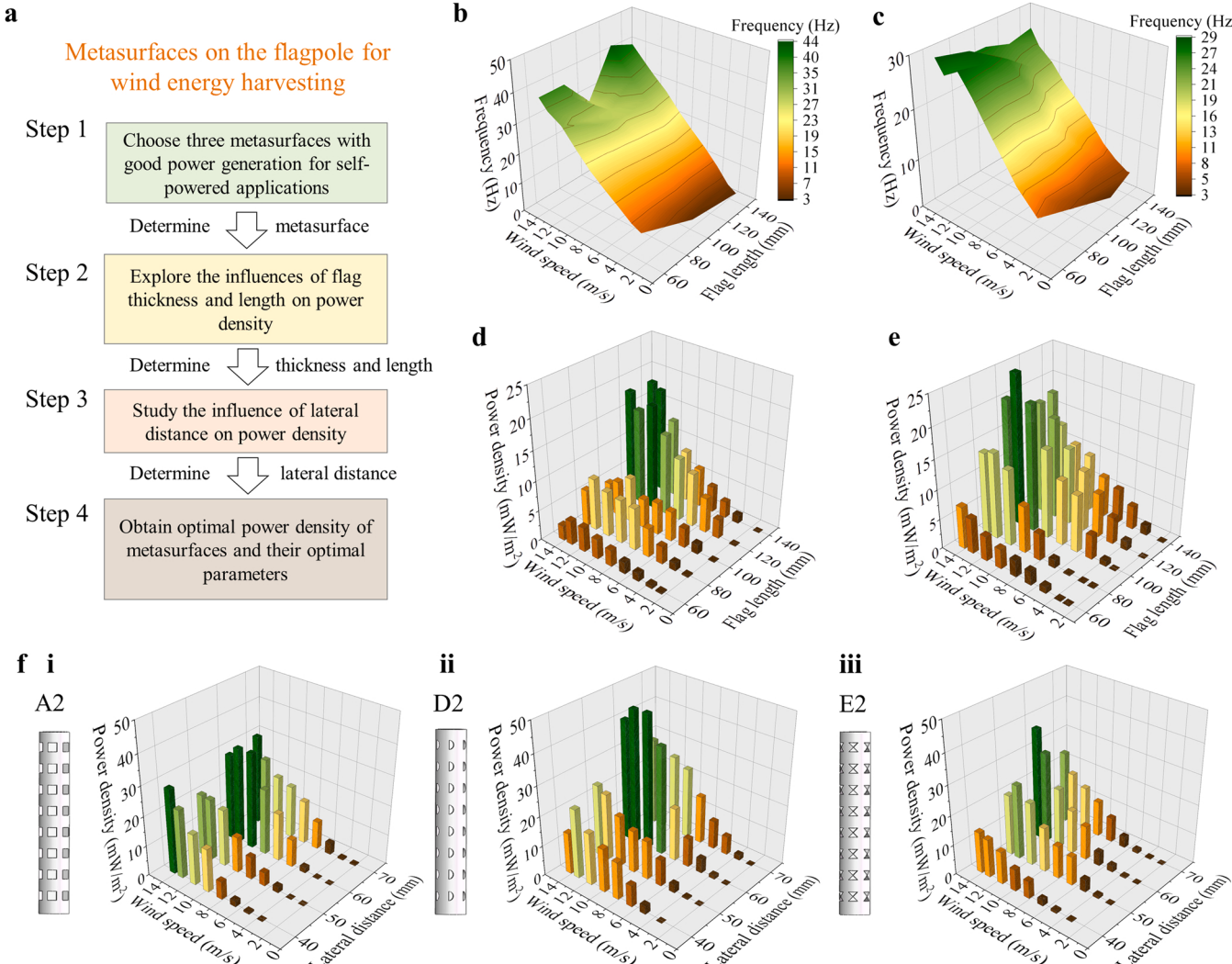


Fig. 5. Metasurfaces on the flagpole for wind energy harvesting: (a) optimization process for FTENGs with metasurfaces towards high-performance wind energy harvesting, (b) fluttering frequency versus wind speed and flag length with 50 μm and (c) 100 μm thickness (Configuration D2); (d) average power density versus wind speed and flag length with 50 μm and (e) 100 μm thickness; (f) average power density of Configurations A2, D2 and E2 versus lateral distance.

metasurface designs on the flagpole in enhancing the wind energy harvesting capacity for FTENGs. Configurations A2, D2 and E2 are chosen for further optimization with the process illustrated in Fig. 5a. Taking Configuration D2 as an example, the effects of different lengths (60–140 mm) and wind speeds (0–15 m/s), with constant thicknesses of 0.05 mm and 0.1 mm, on the fluttering frequency are depicted in Fig. 5b and c. It is observed that the fluttering frequency does not change regularly with the decrease of the flag length (the increase of mass ratio), especially at high-speed winds. This is attributed to the fact that the metasurface and high wind speeds exacerbate the chaotic behavior of the soft flag. The fluttering frequency spectrums of flags with different lengths at 14.4 m/s are illustrated in Fig. S7. When the flag lengths are 140 and 120 mm, the dominant frequency components of flag flutter are relatively concentrated. However, when the flag length is shortened to or below 100 mm, the flutter frequency components are dispersed in the spectrum, which indicates the dominant role of the chaotic behavior.

The thickness of 0.1 mm increases the stiffness of the flag, mitigating this chaotic phenomenon. Meanwhile, the higher mass ratio contributes to lower fluttering frequencies in most conditions compared to a thickness of 0.05 mm. The corresponding power density performance is illustrated in Fig. 5d and e. An optimal flag length of 120 mm, with a thickness of 0.05 mm, yields an average power density of 18.45 mW/m². Meanwhile, for a thickness of 0.1 mm, an optimal average power density of 25.16 mW/m² can be achieved with an optimal length of 100 mm. Therefore, the flag length of 100 mm and the flag thickness of 0.1 mm emerge as the optimal parameters for wind energy harvesting. Importantly, these parameters align with those conducive to high-linearity wind speed sensing, implying that the possibility of FTENG with both high-performance wind energy harvesting and high-linearity speed sensing capabilities. With optimized flag geometric parameters, the power densities of three metasurface configurations are further optimized considering the influence of the lateral distance, as illustrated

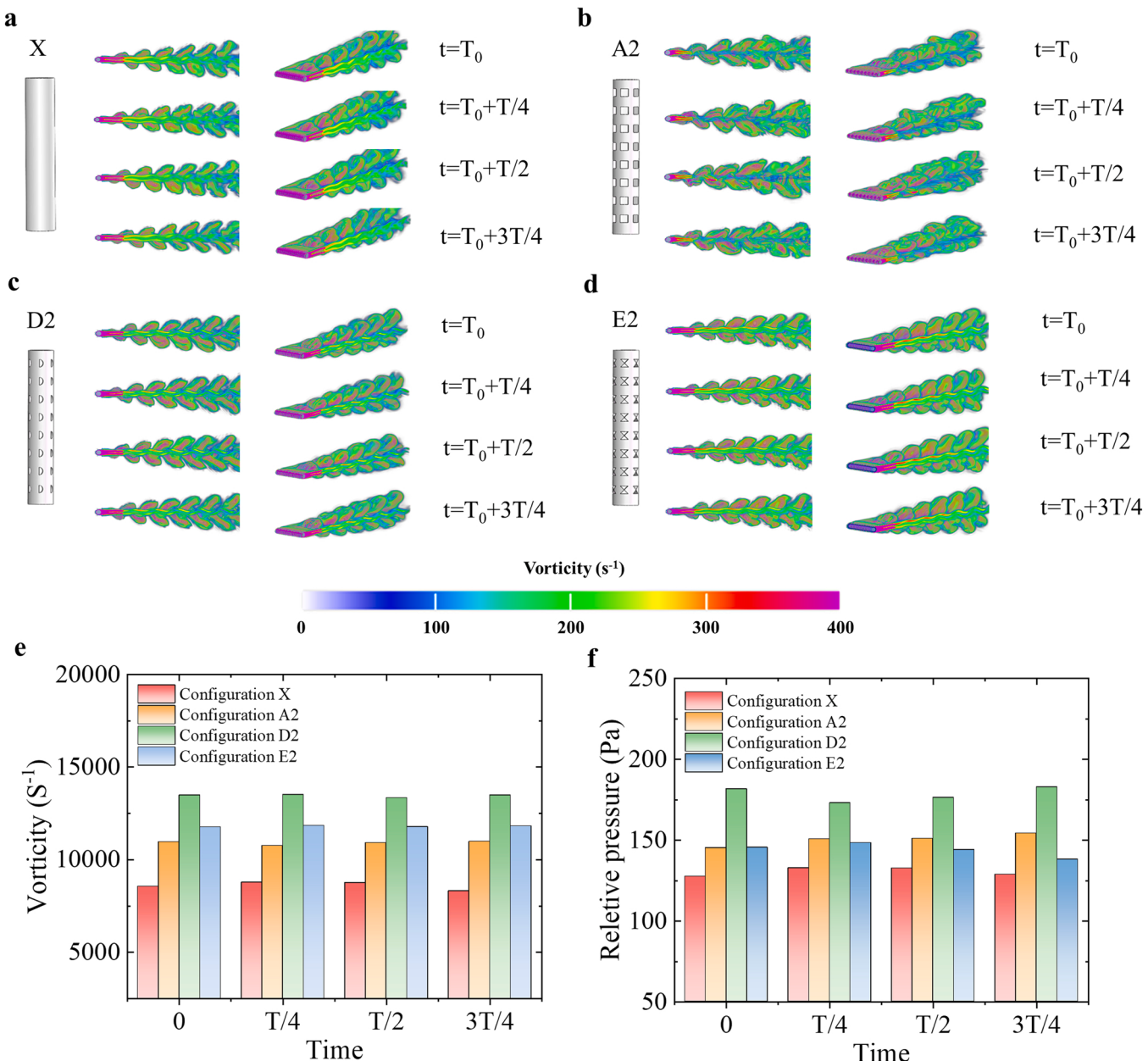


Fig. 6. Vorticity simulation for the flagpoles with the metasurface design at the wind speed of 10 m/s: (a) 3D vorticity simulation for Configuration X, (b) Configuration A2, (c) Configuration D2 and (d) Configuration E2; (e) maximum vorticity values and (f) maximum relative pressure values of characteristic cross-sections of flagpoles in one vortex shedding period (the results are obtained based on the data in a 150 mm × 100 mm flow field region near the metasurface).

in Fig. 5f. They yield an optimal power density of 32.31, 45, and 37.39 mW/m² at the same optimal lateral distance of 60 mm, respectively. Additionally, their corresponding fitness values for wind speed sensing are also presented in Fig. S8.

To comprehensively explore and visually depict the effects of metasurface designs on flagpoles on the surrounding flow field, 3D simulations for flagpoles are conducted using the commercial software XFlow. Fig. 6a-d present the 3D vorticity contours of metasurface designs during the one period of vortex shedding at the wind speed of 10 m/s. To quantify the vortex strength, characteristic cross-sections on four flagpoles are selected (their vorticity contours are illustrated in Fig. S9), and the vorticity and relative pressure data in a flow field region (150 mm × 100 mm) near the metasurface are statistically analyzed and depicted in Fig. 6e and f. Configuration A2 generates more intense vortexes as well as a more pronounced chaos phenomenon in the whole domain (see Figs. 6b and S9b). The vortex strength of Configuration D2 (see Figs. 6c and S9c) is not significantly different from Configurations E2 (see Figs. 6d and S9d) and X (see Figs. 6a and S9a) near the flagpole, but the vortexes in the distance exhibit slower attenuation. From the perspective of the maximum vorticity value in Fig. 6e, the rankings are Configurations E2, D2, and A2, aligning with the optimal power density performance in Fig. 5f(i)-(iii). The vorticities of Configurations D2 and E2 are comparable but higher than that of Configuration X. All three configurations demonstrate at least 30% improvement in the maximum vorticity compared to Configuration X, indicating the metasurface's role in enhancing vorticity. Fig. 6f reflects the vortex strength with the relative pressure. Configuration D2 still gains a maximum pressure, but the difference is the pressure value of Configuration A2 slightly surpasses that of Configuration E2. While the intensified vortexes generated by metasurface designs usually imply a more vigorous influence on the nearby flow fields as well as flow-induced vibrations, this does not entirely determine the energy harvesting performance. The actual performance of FTENG also heavily depends on material properties, geometric parameters, and contact status under the current flow field. The corresponding lift coefficient C_L and drag coefficient C_D are also recorded during the simulation process and presented in Fig. S10.

Based on the above numerous investigation and analysis regarding flagpole diameter, metasurface parameters (diameter, depth/height, and density), metasurface shape designs, flag geometry parameters (thickness and length), and the baffle lateral distance on FTENG performance. A general design guideline is proposed in Fig. S11 to provide some experience for similar designs towards single or multiple application purposes, and general optimization steps are supplemented in Note S2.

2.6. Power optimization for FTENG

Fig. 7a provides a comprehensive evaluation of FTENGs from perspectives of linearity, operational range, power density and its corresponding wind speed, and device volume, to seek a candidate capable of both high-performance wind energy harvesting and high-linearity wind speed sensing. All candidates are optimized and configured with corresponding parameters for achieving maximum power density. Among the optimized candidates, Configuration D1 exhibits the best linearity of 0.999 and the broadest operational bandwidth spanning a wind speed range of 12.37 m/s, while the average power density is limited to 30.16 mW/m². On the other hand, Configuration D2 achieves the highest power density of 45.26 mW/m² and maintains a good linearity of 0.992 for wind speed sensing. Considering a tiny difference in the linearity and operational range, Configuration D2 is considered as the most optimal choice for balancing wind energy harvesting and speed sensing, and its open-circuit voltage and short-circuit current after parameter optimization are presented in Figs. S12 and S13. To further explore the potential of Configuration D2, impedance matching tests are conducted. In Figs. 7b and S14, the FTENG achieves an average/peak power density of 11.5/22.3 and 34.31/89.41 mW/m² with an optimal resistance of 45 MΩ at wind speeds of 6.7 and 10 m/s. At a wind speed of 13.3 m/s, the average/peak power density reaches 52.95/218.9 mW/m² along with a slightly increased resistance of 50 MΩ. As illustrated in Fig. 7c, the optimized Configuration D2 significantly enhances the performance of breeze energy harvesting, achieving up to a 10 times improvement compared to the original Configuration X. Even under

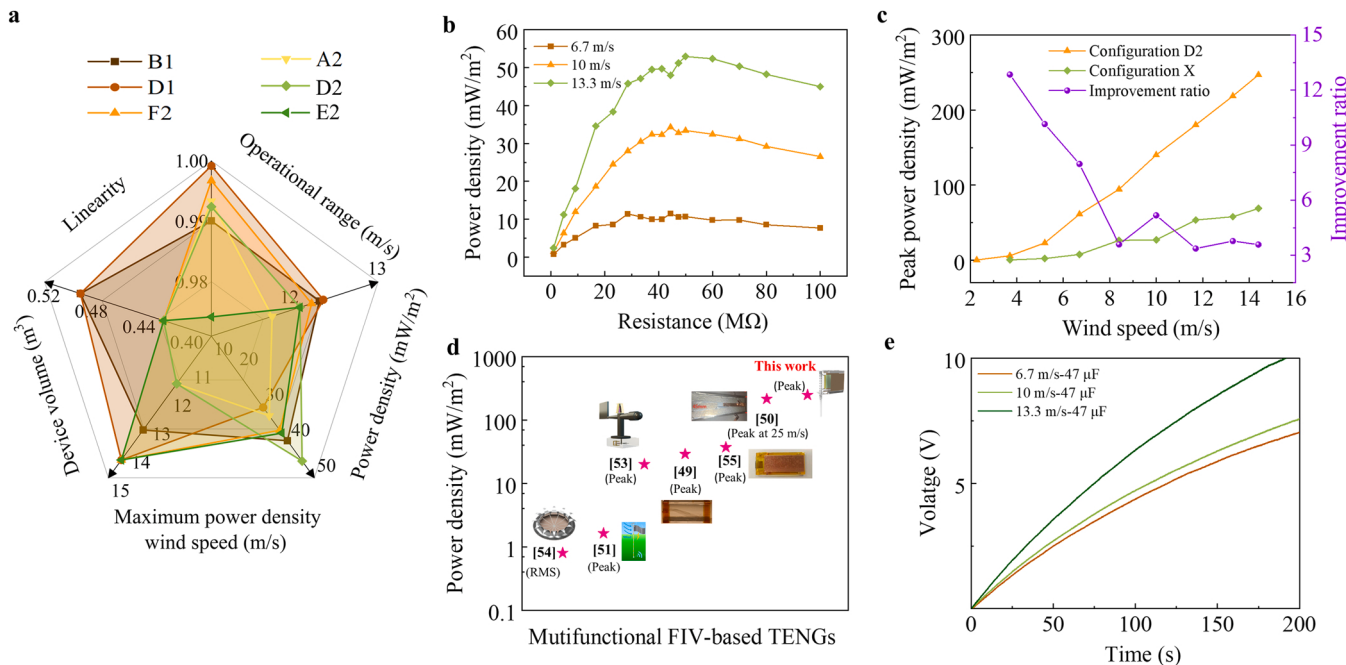


Fig. 7. Performance evaluation and optimization for the FTENG: (a) Comprehensive comparison of optimized FTENGs with different metasurface designs from the perspectives of linearity, operational range, power density its corresponding wind speed, and device volume; (b) average power density of the optimized Configuration D2 versus external resistance; (c) comparison of the peak power density between Configuration D2 and original Configuration X; (d) comparison of the power density of multifunctional FIV-based TENGs; (e) capacitor charging tests for optimized Configuration D2.

high-speed wind conditions, the boost can be maintained at 3.4–5.2 times. Notably, a peak power density of 250 mW/m² is achieved at 14.4 m/s, which is a remarkable performance compared to similar multifunctional FIV-based TENGs in Fig. 7d. In addition, the wind speed sensing capacity of proposed FTENG is outstanding in TENG-based wind

speed sensors, as shown in Fig. S15. Fig. 7e presents the performance of FTENG with Configuration D2 for charging a capacitor. A faster charging speed, compared to that at low and middle wind speeds, is attained at 13.3 m/s, only taking 75 seconds for the 47 μ F capacitor charged to 5 V. Fig. S16 illustrates the surface charge test result for PTFE membrane. At

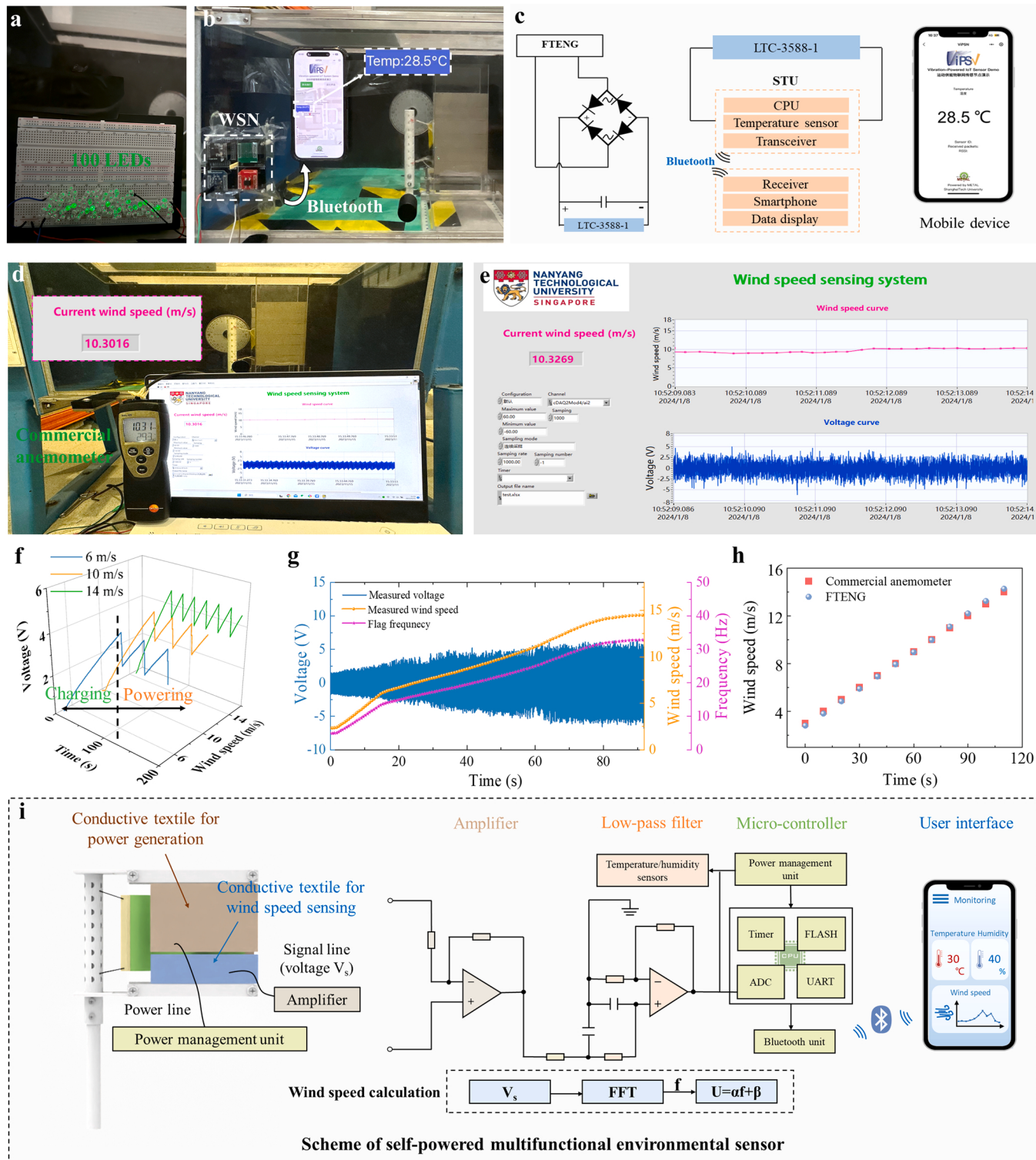


Fig. 8. Demonstrations for FTENG in self-powered systems and environmental signal sensing: (a) LED lighting test; (b) demonstration of FTENG powering a WSN and (c) scheme of the mobile temperature monitoring; (d) demonstration of FTENG as a wind speed sensor and (e) wind speed sensing interface; (f) voltage curve of the interface circuit when powering the temperature sensor; (g) measured voltage, calculated flag fluttering frequency and corresponding wind speed during the wind speed sensing; (h) comparison of the FTENG and a commercial anemometer in wind speed sensing; (i) scheme of self-powered multifunctional environmental sensing system based on the FTENG with a metasurface design.

the wind speed of 10 m/s, the uncharged PTFE film reaches a stable state with 96 seconds. Durability is a key indicator determining the reliability of TENG in practical applications. As shown in Fig. S17, there is no significantly decrease in the FTENG output after 300,000 cycles in the durability test.

2.7. Demonstration of FTENG as a self-powered WSN and wind speed sensor

In this section, the FTENG will demonstrate its applications in self-powered systems and wind speed sensing. As shown in Fig. 8a, the FTENG operates at a wind speed of 10 m/s lighting 100 LEDs in series, demonstrating its potential in powering electronics that require instantaneous high power. Fig. 8b presents a photograph of the FTENG powering a WSN implementing temperature monitoring on mobile devices via Bluetooth technology. The integrated energy harvesting circuit with WSN is detailed in Fig. S18, and the detailed self-powered scheme is illustrated in Fig. 8c. The energy harvesting circuit incorporates a rectifier unit, a filter capacitor, a power management unit, and a signal transmission unit. The alternating voltage generated by the FTENG is first input to the rectifier unit and stabilized as a direct voltage with the filter capacitor. Then, the power management unit designed based on a commercial chip LTC-3588-1 will govern the input electricity and guarantee low-power operation. The available electrical energy will be finally exploited to power the signal transmission unit including the CPU, signal transmitter, and temperature sensor. In Fig. 8f, the voltage of the interface circuit when powering the signal transmission unit and temperature sensor is charged to 5 V first during the FTENG operation. Subsequently, with the switch turned on, the electrical energy is transferred to the signal transmission unit. The power interval, varying with wind speed, can be maintained at 20–40 s. A visual demonstration of the self-powered WSN is provided in Video S1.

Supplementary material related to this article can be found online at doi:10.1016/j.nanoen.2024.109508.

The photograph of the FTENG employed as a high-linearity wind speed sensor is depicted in Fig. 8d, along with a detailed view of the developed wind speed sensing interface based on LabVIEW presented in Fig. 8e (its internal operation logic is shown in Fig. S19). The measurement accuracy and response speed of FTENG are compared with a commercial anemometer in Video S2. In the video, the wind speed sensed by the FTENG closely follows the changes in actual wind speed and exhibits high consistency with the anemometer in measured values. Fig. 8g illustrates the sensing range of the TENG-based wind speed sensor and its corresponding measured voltage signal, indicating an effective range of 2.3–14.4 m/s. In addition, Fig. 8h compares the FTENG and a commercial anemometer at multiple wind speeds, indicating the superior measurement accuracy of the FTENG. Based on various demonstration tests, Fig. 8i envisions a battery-free sensing system monitoring wind speed and other ambient signals. The electrodes, fixed on the inner side of the baffles, are divided into two parts for energy harvesting and speed sensing, respectively. The large part is exploited for energy harvesting, and the harnessed energy is processed by the power management unit to power the temperature/humidity sensors and the microcontroller. Simultaneously, the voltage signal generated by the small part is employed for wind speed sensing, processed by an amplifier, and low-pass filter, and transmitted to the analog-to-digital converter (ADC). The microcontroller accounts for the wind speed calculation with the CPU, and the transmission of the wind speed, temperature, and humidity signals with the Bluetooth unit, thus implementing mobile monitoring based on the battery-free sensing system.

Supplementary material related to this article can be found online at doi:10.1016/j.nanoen.2024.109508.

3. Conclusions

In summary, this study aims to simultaneously enhance the wind energy harvesting and wind speed sensing capabilities of the FTENG by utilizing a metasurface design, thereby achieving the abilities to power WSNs and function as a self-powered wind speed sensor. By employing a flexible fixing approach and metasurface design to maximize the harnessing of upstream wakes, a significant power density enhancement of up to 23 times was achieved. A total of 12 metasurface designs were developed and compared. Among them, the device parameters of Configurations B1, D1 and F2 were further optimized for the application of sensing, and the fluttering frequency of the optimized Configuration D1 versus wind speed demonstrated an outstanding fitness of 0.999, indicating a high-linearity wind speed sensing capacity. In addition, Configurations A2, D2 and E2 were further optimized for wind energy harvesting, with Configuration D2 emerging as the most promising candidate, achieving the highest average power density of 45 mW/m² and a peak power of 250 mW/m². Notably, Configuration D2 also exhibited a considerable fitness of 0.992 across a wind speed range of 2.3–14.4 m/s, positioning it as a favorable choice for multifunctional FTENGs. A series of tests showcased the versatile capabilities of the FTENG, demonstrating the abilities to instantaneously light 100 LEDs, power a WSN with a power interval of 20–40 s at variable wind speeds, and serve effectively as an environmental sensor. The FTENG-based wind speed sensor possesses a superior response and measurement accuracy highly consistent with a commercial anemometer. Furthermore, through optimized FTENG electrode design and the integration of electronic sensing components, it is possible to achieve precise and multifunctional self-powered monitoring of environmental parameters, including wind speed, temperature, humidity, and others. The metasurface design on the flagpole offers an effective and easily implementable approach to modulate the performance of FTENGs, enabling versatile applications of self-powered electronics.

4. Experimental section

4.1. Fabrication of FTENG

The flag body in the FTENG was made of the PTFE membrane. The baffles were manufactured with acrylic material, and the Nickel-coated conductive textile was fixed on their inside. The flagpole consisting of two cylinders was made of polylactide material by 3D printing technology. The upper part with a metasurface design possessed a diameter of 30 mm and a height of 150 mm. The concave depth or convex height of metasurface characteristics was 5 mm, and the characteristic length or diameter of metasurface design was 6 mm. The diameter and height of the below part of the flagpole were 15 and 50 mm. The composition and assembly of FTENG is presented in Video S3.

Supplementary material related to this article can be found online at doi:10.1016/j.nanoen.2024.109508.

4.2. Characterization and signal measurement of FTENG

The performance validation for the FTENG was conducted with a wind tunnel (FM670 from EdLabQUIP) in the CEE Protective Engineering Lab of Nanyang Technological University. The maximum wind speed of the wind tunnel is 15 m/s and the cross section is 300 × 300 mm². An oscilloscope with a model of Tektronix MSO44 was employed to measure the generated voltage signal of FTENG. To ensure the consistency of surface charge densities of FTENGs to the greatest extent possible, the PTFE flag and conductive textiles remained unchanged during the testing of all metasurface configurations illustrated in Fig. 3. Additionally, the operator wore rubber gloves throughout the testing process. As depicted in Fig. S2, we utilized separated baffles internally lined with conductive textiles to maintain consistency in the triboelectric surfaces during each test. Furthermore, after the

completion of testing for each metasurface configuration, the PTFE flag was replaced with another metasurface flagpole. Following replacement, the PTFE flag was subjected to a speed of 10 m/s for a few minutes to ensure full charging. Subsequently, the output voltage of the FTENG with the newly configured metasurface was tested and recorded. The voltage performances of different metasurface configurations were then compared with the average values obtained from three tests. A resistance substitute (IET RS-200 W) and a capacitance substitute (IET RCS-500) were exploited to find the optimal resistance and validate the capacitor charging performance of FTENG. The NI USB-9229 acquisition card was used for capturing voltage signals in the wind speed sensing demonstration, and the wind speed sensing interface was developed based on the commercial software LabVIEW.

CRediT authorship contribution statement

Liwei Dong: Writing – review & editing, Writing – original draft, Validation, Software, Methodology, Conceptualization. **Guobiao Hu:** Validation, Software, Formal analysis. **Ye Zhang:** Validation, Software, Resources. **Wei Ding:** Writing – review & editing, Visualization, Formal analysis, Data curation. **Shuai Qu:** Writing – review & editing, Software, Methodology. **Qian Tang:** Writing – review & editing, Validation, Resources, Methodology, Formal analysis. **Chaoyang Zhao:** Supervision, Resources, Project administration. **Yaowen Yang:** Writing – review & editing, Supervision, Project administration, Methodology, Funding acquisition, Conceptualization. **Fan Yang:** Writing – review & editing, Validation, Methodology, Formal analysis, Conceptualization.

Declaration of Competing Interest

The authors declare that they have no known competing financial interests or personal relationships that could have appeared to influence the work reported in this paper.

Data availability

Data will be made available on request.

Acknowledgments

This research is sponsored by the National Natural Science Foundation of China (Grant No. 12202276), Shanghai Pujiang Program (Grant No. 22PJ1412500), NTU grant 020671-00001. The first author acknowledges the financial support from the China Scholarship Council (Grant No. 202206260157) for supporting his joint training Ph.D. program at Nanyang Technological University.

Appendix A. Supporting information

Supplementary data associated with this article can be found in the online version at [doi:10.1016/j.nanoen.2024.109508](https://doi.org/10.1016/j.nanoen.2024.109508).

References

- [1] Y. Qin, X. Wang, Z.L. Wang, Microfibre–nanowire hybrid structure for energy scavenging, *Nature* 451 (2008) 809–813.
- [2] L.-C. Zhao, H.-X. Zou, K.-X. Wei, S.-X. Zhou, G. Meng, W.-M. Zhang, Mechanical Intelligent Energy Harvesting: From Methodology to Applications, *Adv. Energy Mater.* 13 (2023) 2300557.
- [3] B. Yu, J. Duan, H. Cong, W. Xie, R. Liu, X. Zhuang, H. Wang, B. Qi, M. Xu, Z. L. Wang, J. Zhou, Thermosensitive crystallization–boosted liquid thermocells for low-grade heat harvesting, *Science* 370 (2020) 342–346.
- [4] W.J. Jang, H.W. Jang, S.Y. Kim, Recent Advances in Wide Bandgap Perovskite Solar Cells: Focus on Lead-Free Materials for Tandem Structures, *Small Methods* (2023) 2300207.
- [5] C. Shan, W. He, H. Wu, S. Fu, K. Li, A. Liu, Y. Du, J. Wang, Q. Mu, B. Liu, Y. Xi, C. Hu, Dual Mode TENG with Self-Voltage Multiplying Circuit for Blue Energy Harvesting and Water Wave Monitoring, *Adv. Funct. Mater.* 33 (2023) 2305768.
- [6] U. Khan, S.-W. Kim, Triboelectric Nanogenerators for Blue Energy Harvesting, *ACS Nano* 10 (2016) 6429–6432.
- [7] L. Dong, G. Hu, J. Yu, C. Zhao, S. Qu, Y. Yang, Maximizing onboard power generation of large-scale railway vibration energy harvesters with intricate vehicle-harvester-circuit coupling relationships, *Appl. Energy* 347 (2023) 121388.
- [8] W. Wu, X. Cao, J. Zou, Y. Ma, X. Wu, C. Sun, M. Li, N. Wang, Z. Wang, L. Zhang, Triboelectric Nanogenerator Boosts Smart Green Tires, *Adv. Funct. Mater.* 29 (2019) 1806331.
- [9] L. Dong, J. Zuo, T. Wang, W. Xue, P. Wang, J. Li, F. Yang, Enhanced piezoelectric harvester for track vibration based on tunable broadband resonant methodology, *Energy* 254 (2022) 124274.
- [10] X. Hou, M. Zhu, L. Sun, T. Ding, Z. Huang, Y. Shi, Y. Su, L. Li, T. Chen, C. Lee, Scalable self-attaching/assembling robotic cluster (S2A2RC) system enabled by triboelectric sensors for in-orbit spacecraft application, *Nano Energy* 93 (2022) 106894.
- [11] L. Dong, J. Li, H. Zhang, M. Gao, Y. Yang, F. Yang, Adaptive energy harvesting approach for smart wearables towards human-induced stochastic oscillations, *J. Clean. Prod.* 418 (2023) 138094.
- [12] C. Chen, H. Guo, L. Chen, Y.-C. Wang, X. Pu, W. Yu, F. Wang, Z. Du, Z.L. Wang, Direct Current Fabric Triboelectric Nanogenerator for Biomotion Energy Harvesting, *ACS Nano* 14 (2020) 4585–4594.
- [13] J. Zuo, L. Dong, F. Yang, Z. Guo, T. Wang, L. Zuo, Energy harvesting solutions for railway transportation: A comprehensive review, *Renew. Energy* 202 (2023) 56–87.
- [14] F.-R. Fan, Z.-Q. Tian, Z. Lin Wang, Flexible triboelectric generator, *Nano Energy* 1 (2012) 328–334.
- [15] H. Fu, X. Mei, D. Yurchenko, S. Zhou, S. Theodossiades, K. Nakano, E.M. Yeatman, Rotational energy harvesting for self-powered sensing, *Joule* 5 (2021) 1074–1118.
- [16] L. He, C. Zhang, B. Zhang, O. Yang, W. Yuan, L. Zhou, Z. Zhao, Z. Wu, J. Wang, Z. L. Wang, A Dual-Mode Triboelectric Nanogenerator for Wind Energy Harvesting and Self-Powered Wind Speed Monitoring, *ACS Nano* 16 (2022) 6244–6254.
- [17] B. Zhang, C. Zhang, O. Yang, W. Yuan, Y. Liu, L. He, Y. Hu, Z. Zhao, L. Zhou, J. Wang, Z.L. Wang, Self-Powered Seawater Electrolysis Based on a Triboelectric Nanogenerator for Hydrogen Production, *ACS Nano* 16 (2022) 15286–15296.
- [18] J. Wang, D. Yurchenko, G. Hu, L. Zhao, L. Tang, Y. Yang, Perspectives in flow-induced vibration energy harvesting, *Appl. Phys. Lett.* 119 (2021).
- [19] A.M. Tairab, X. Wang, Z. Zhang, D. Hao, M. Abdelrahman, W. Salman, A. Ali, The Nexus of IoT technology: A renewable multi-module energy harvester for self-powered on railway, *Sustain. Mater. Technol.* 38 (2023) e00752.
- [20] H. Cao, M. Tang, Z. Zhang, A.M. Tairab, H. Mutusuda, X. Wu, A magnetic coupling wind energy harvester for unmanned surface vehicles, *Int. J. Mech. Sci.* 257 (2023) 108543.
- [21] L.-C. Zhao, H.-X. Zou, G. Yan, F.-R. Liu, T. Tan, K.-X. Wei, W.-M. Zhang, Magnetic coupling and flexextensional amplification mechanisms for high-robustness ambient wind energy harvesting, *Energy Convers. Manag.* 201 (2019) 112166.
- [22] Y. Wang, X. Liu, T. Chen, H. Wang, C. Zhu, H. Yu, L. Song, X. Pan, J. Mi, C. Lee, M. Xu, An underwater flag-like triboelectric nanogenerator for harvesting ocean current energy under extremely low velocity condition, *Nano Energy* 90 (2021) 106503.
- [23] W. Liu, Z. Wang, G. Wang, G. Liu, J. Chen, X. Pu, Y. Xi, X. Wang, H. Guo, C. Hu, Z. L. Wang, Integrated charge excitation triboelectric nanogenerator, *Nat. Commun.* 10 (2019) 1426.
- [24] J. Wang, C. Wu, Y. Dai, Z. Zhao, A. Wang, T. Zhang, Z.L. Wang, Achieving ultrahigh triboelectric charge density for efficient energy harvesting, *Nat. Commun.* 8 (2017) 88.
- [25] D.-J. Sun, W.-Z. Song, C.-L. Li, T. Chen, D.-S. Zhang, J. Zhang, S. Ramakrishna, Y.-Z. Long, High-voltage direct current triboelectric nanogenerator based on charge pump and air ionization for electrospinning, *Nano Energy* 101 (2022) 107599.
- [26] L. Long, W. Liu, Z. Wang, W. He, G. Li, Q. Tang, H. Guo, X. Pu, Y. Liu, C. Hu, High performance floating self-excited sliding triboelectric nanogenerator for micro mechanical energy harvesting, *Nat. Commun.* 12 (2021) 4689.
- [27] C. Ye, K. Dong, J. An, J. Yi, X. Peng, C. Ning, Z.L. Wang, A Triboelectric-Electromagnetic Hybrid Nanogenerator with Broadband Working Range for Wind Energy Harvesting and a Self-Powered Wind Speed Sensor, *ACS Energy Lett.* 6 (2021) 1443–1452.
- [28] K.-J.I. Egbe, A. Matin Nazar, P. Jiao, Piezoelectric-triboelectric-electromagnetic Hybrid Rotational Energy Harvesters (H-REH), *Int. J. Mech. Sci.* 235 (2022) 107722.
- [29] L.-C. Zhao, H.-X. Zou, G. Yan, F.-R. Liu, T. Tan, W.-M. Zhang, Z.-K. Peng, G. Meng, A water-proof magnetically coupled piezoelectric-electromagnetic hybrid wind energy harvester, *Appl. Energy* 239 (2019) 735–746.
- [30] J.-A. Choi, J. Jeong, M. Kang, H.-J. Ko, T. Kim, K. Park, J. Kim, S. Pyo, Externally motionless triboelectric nanogenerator based on vortex-induced rolling for omnidirectional wind energy harvesting, *Nano Energy* 119 (2024) 109071.
- [31] J. Wang, L. Geng, L. Ding, H. Zhu, D. Yurchenko, The state-of-the-art review on energy harvesting from flow-induced vibrations, *Appl. Energy* 267 (2020) 114902.
- [32] H. Li, J. Wen, Z. Ou, E. Su, F. Xing, Y. Yang, Y. Sun, Z.L. Wang, B. Chen, Leaf-Like TENGs for Harvesting Gentle Wind Energy at An Air Velocity as Low as 0.2 m s⁻¹, *Adv. Funct. Mater.* 33 (2023) 221207.
- [33] B. Zhang, B. Li, S. Fu, Z. Mao, W. Ding, Vortex-Induced Vibration (VIV) hydrokinetic energy harvesting based on nonlinear damping, *Renew. Energy* 195 (2022) 1050–1063.
- [34] A. Abdelkefi, J.M. Scanlon, E. McDowell, M.R. Hajj, Performance enhancement of piezoelectric energy harvesters from wake galloping, *Appl. Phys. Lett.* 103 (2013).
- [35] A. Barrero-Gil, G. Alonso, A. Sanz-Andres, Energy harvesting from transverse galloping, *J. Sound Vib.* 329 (2010) 2873–2883.

- [36] J.M. McCarthy, S. Watkins, A. Deivasigamani, S.J. John, Fluttering energy harvesters in the wind: A review, *J. Sound Vib.* 361 (2016) 355–377.
- [37] J. Wang, S. Sun, G. Hu, Y. Yang, L. Tang, P. Li, G. Zhang, Exploring the potential benefits of using metasurface for galloping energy harvesting, *Energy Convers. Manag.* 243 (2021) 114414.
- [38] M. Usman, A. Hanif, I.-H. Kim, H.-J. Jung, Experimental validation of a novel piezoelectric energy harvesting system employing wake galloping phenomenon for a broad wind spectrum, *Energy* 153 (2018) 882–889.
- [39] L. Ding, L. Zhang, C. Wu, X. Mao, D. Jiang, Flow induced motion and energy harvesting of bluff bodies with different cross sections, *Energy Convers. Manag.* 91 (2015) 416–426.
- [40] J. Liu, B. Bao, J. Chen, Y. Wu, Q. Wang, Passively adaptive wind energy harvester featuring a double-airfoil bluff body with adjustable attack angles, *Mech. Syst. Signal Process.* 185 (2023) 109814.
- [41] Z. Zhao, X. Pu, C. Du, L. Li, C. Jiang, W. Hu, Z.L. Wang, Freestanding Flag-Type Triboelectric Nanogenerator for Harvesting High-Altitude Wind Energy from Arbitrary Directions, *ACS Nano* 10 (2016) 1780–1787.
- [42] Y. Zou, M. Sun, F. Yan, T. Du, Z. Xi, F. Li, C. Zhu, H. Wang, J. Zhao, P. Sun, M. Xu, A High-Performance Flag-Type Triboelectric Nanogenerator for Scavenging Wind Energy toward Self-Powered IoTs, *Materials* 15 (2022).
- [43] B. Cheng, C. Qi, Y. Ding, X. Jia, S. Bai, Q. Xu, Y. Yu, J. Wen, Y. Qin, High output performance flutter-driven triboelectric nanogenerator, *Nano Energy* 106 (2023) 108106.
- [44] J. Bae, J. Lee, S. Kim, J. Ha, B.-S. Lee, Y. Park, C. Choong, J.-B. Kim, Z.L. Wang, H.-Y. Kim, J.-J. Park, U.I. Chung, Flutter-driven triboelectrification for harvesting wind energy, *Nat. Commun.* 5 (2014) 4929.
- [45] U. Latif, M.Y. Younis, S. Idrees, E. Uddin, A. Abdelkefi, A. Munir, M. Zhao, Synergistic analysis of wake effect of two cylinders on energy harvesting characteristics of piezoelectric flag, *Renew. Sustain. Energy Rev.* 173 (2023) 113114.
- [46] U. Latif, E.H. Dowell, E. Uddin, M. Yamin, Younis, Parametric aerodynamic and aeroelastic study of a deformable flag-based energy harvester for powering low energy devices, *Energy Convers. Manag.* 280 (2023) 116846.
- [47] L. Dong, Q. Tang, C. Zhao, G. Hu, S. Qu, Z. Liu, Y. Yang, Flag-type hybrid nanogenerator utilizing flapping wakes for consistent high performance over an ultra-broad wind speed range, *Nano Energy* 119 (2024) 109057.
- [48] Y. Han, F. Wu, X. Du, Z. Li, H. Chen, D. Guo, J. Wang, H. Yu, Enhance vortices vibration with Y-type bluff body to decrease arousing wind speed and extend range for flag triboelectric energy harvester, *Nano Energy* 119 (2024) 109063.
- [49] Y. Yang, G. Zhu, H. Zhang, J. Chen, X. Zhong, Z.-H. Lin, Y. Su, P. Bai, X. Wen, Z. L. Wang, Triboelectric Nanogenerator for Harvesting Wind Energy and as Self-Powered Wind Vector Sensor System, *ACS Nano* 7 (2013) 9461–9468.
- [50] Y. Liu, J. Liu, L. Che, A. High, Sensitivity Self-Powered Wind Speed Sensor Based on Triboelectric Nanogenerators (TENGs), *Sensors* 21 (2021) 2951.
- [51] Y. Wang, E. Yang, T. Chen, J. Wang, Z. Hu, J. Mi, X. Pan, M. Xu, A novel humidity resisting and wind direction adapting flag-type triboelectric nanogenerator for wind energy harvesting and speed sensing, *Nano Energy* 78 (2020) 105279.
- [52] Y. Yao, Z. Zhou, K. Wang, Y. Liu, X. Lu, T. Cheng, Arc-shaped flutter-driven wind speed sensor based on triboelectric nanogenerator for unmanned aerial vehicle, *Nano Energy* 104 (2022) 107871.
- [53] Q. Xu, Y. Lu, S. Zhao, N. Hu, Y. Jiang, H. Li, Y. Wang, H. Gao, Y. Li, M. Yuan, L. Chu, J. Li, Y. Xie, A wind vector detecting system based on triboelectric and photoelectric sensors for simultaneously monitoring wind speed and direction, *Nano Energy* 89 (2021) 106382.
- [54] H.-J. Ko, D.-S. Kwon, S. Pyo, J. Kim, Curved flap array-based triboelectric self-powered sensor for omnidirectional monitoring of wind speed and direction, *Nano Energy* 102 (2022) 107717.
- [55] X. Yu, S. Fu, X. Zuo, J. Zeng, C. Shan, W. He, W. Li, C. Hu, Moisture Resistant and Stable Wireless Wind Speed Sensing System Based on Triboelectric Nanogenerator with Charge-Excitation Strategy, *Adv. Funct. Mater.* 32 (2022) 2207498.
- [56] S. Niu, Y. Liu, X. Chen, S. Wang, Y.S. Zhou, L. Lin, Y. Xie, Z.L. Wang, Theory of freestanding triboelectric-layer-based nanogenerators, *Nano Energy* 12 (2015) 760–774.
- [57] B.S.H. Connell, D.K.P. Yue, Flapping dynamics of a flag in a uniform stream, *J. Fluid Mech.* 581 (2007) 33–67.
- [58] S. Orrego, K. Shoele, A. Ruas, K. Doran, B. Caggiano, R. Mittal, S.H. Kang, Harvesting ambient wind energy with an inverted piezoelectric flag, *Appl. Energy* 194 (2017) 212–222.